

From metallic glasses to nanocrystals: Molecular dynamics simulations on the crossover from glass-like to grain-boundary-mediated deformation behaviour

Tobias Brink^{1,*}, Karsten Albe

*Fachgebiet Materialmodellierung, Institut für Materialwissenschaft,
Technische Universität Darmstadt, Otto-Berndt-Straße 3, D-64287 Darmstadt, Germany*

Abstract

Nanocrystalline metals contain a large fraction of high-energy grain boundaries, which may be considered as glassy phases. Consequently, with decreasing grain size, a crossover in the deformation behaviour of nanocrystals to that of metallic glasses has been proposed. Here, we study this crossover using molecular dynamics simulations on bulk glasses, glass-crystal nanocomposites, and nanocrystals of $\text{Cu}_{64}\text{Zr}_{36}$ with varying crystalline volume fractions induced by long-time thermal annealing. We find that the grain boundary phase behaves like a metallic glass under constraint from the abutting crystallites. The transition from glass-like to grain-boundary-mediated plasticity can be classified into three regimes: (1) For low crystalline volume fractions, the system resembles a glass-crystal composite and plastic flow is localised in the amorphous phase; (2) with increasing crystalline volume fraction, clusters of crystallites become jammed and the mechanical response depends critically on the relaxation state of the glassy grain boundaries; (3) at grain sizes ≥ 10 nm, the system is jammed completely, prohibiting pure grain-boundary plasticity and instead leading to co-deformation. We observe an inverse Hall-Petch effect only in the second regime when the grain boundary is not deeply relaxed. Experimental results with different grain boundary states are therefore not directly comparable in this regime.

Keywords: Metallic glass, Nanocomposite, Nanocrystalline metals, Grain boundaries, Molecular dynamics simulations

1. Introduction

Deformation mechanisms operating in nanocrystalline metals sensitively depend on the average grain size and grain size distribution [1]. In contrast to coarse-grained polycrystalline metals, where plastic strain is predominantly carried by dislocations, grain-boundary-mediated deformation processes (including sliding and shuffling mechanisms) become increasingly relevant with decreasing grain size. Since the first controlled synthesis of nanocrystalline metals in the late 1980s [2], a large body of literature on the nature of deformation mechanisms in this material class has appeared, which eventually led to the development of deformation maps showing active mechanisms as a function of grain size, temperature, or strain rate (see Ref. 3 for an overview). Since low-energy grain boundaries are typically absent in nanocrystalline microstructures [3], several studies have fostered the view that a nanocrystalline metal could also be considered as a composite of a glassy, percolating grain boundary phase confined between nanocrystallites

[4, 5]. Thus, a smooth transition to glass-like deformation behaviour could be expected with decreasing grain size (see Fig. 1). The parallels between grain boundary deformation and the deformation mechanisms in metallic glasses (MGs)

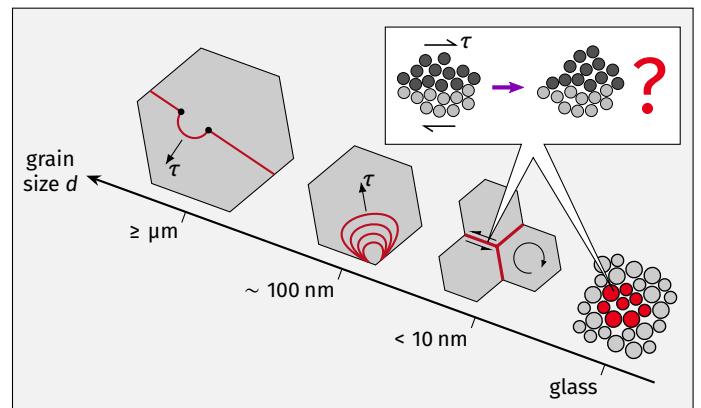


Figure 1: Transition from nanocrystals to metallic glasses. While coarse-grained polycrystals exhibit classical, bulk-like dislocation activity, deformation mechanisms in nanocrystals depend on the average grain size. Grain boundaries act as sinks and sources for dislocation activity, and the plasticity of the grain boundaries themselves becomes important in the sub-10-nm regime. With further decrease of the grain size d , a transition to deformation behaviour known from glasses was postulated: Experimental data indicate similarities between shear transformations in glasses and grain boundary plasticity, suggesting a smooth transition to the glassy state at small d .

*Corresponding author

Email address: brink@mm.tu-darmstadt.de (Tobias Brink)

¹Present address: *Civil Engineering Institute and Institute of Materials Science and Engineering, École polytechnique fédérale de Lausanne (EPFL), Station 18, CH-1015 Lausanne, Switzerland*

are indeed striking: MGs deform via shear-transformation zones (STZs), small regions in which a shear deformation is activated under external stress [6, 7]. Similar concepts have been applied to grain boundaries [8, 9] and yielding in nanocrystals has been shown to exhibit a $T^{2/3}$ temperature dependence [10], just as described for MGs by Johnson and Samwer [11]. Trelewicz and Schuh performed nanoindentation experiments on very small-grained Ni–W alloys and found that they show pop-in events similar to those observed in indentation on metallic glasses [5]. Moreover, the indents featured shear offsets in the surrounding pile-up, indicative of shear banding. An extrapolation of these indentation testing data with varying grain sizes arrives at the amorphous limit [5, 12, 13], estimated at around 1 nm and supported by simulations that report a collapse of the crystalline lattice at such small grain sizes [14–16]. It was also conclusively shown by experiment and computer simulations that the grain boundary phase is characterised by a lower shear modulus, which starts affecting the effective macroscopic shear modulus [17, 18], making the structure reminiscent of the liquid-like/solid-like division in metallic glasses [19–22].

A problem with the experimental data, which was mostly obtained for Ni–W systems, is that the grain size can only be controlled by varying the tungsten content [5, 12, 13]. Pure systems exhibit rapid grain growth even at room temperature [23, 24]. By segregation of solutes to the grain boundaries, small grain sizes can be stabilised [13, 25–30], even in miscible systems [31, 32]. As a result, though, not only the grain size but also the nature of the grain boundary itself may be modified [30, 33–37]. Therefore, any quantitative trend extracted experimentally from varying grain sizes below 10 nm has to be interpreted with care, since the grain boundary state and composition also changes with grain size.

If we accept at this point the proposition of glass-like grain boundaries, we could also consider a nanocrystal as one limit of a glass–crystal nanocomposite. Such composites have received a lot of attention for their potential to retain the high yield strength and large elastic limit of MGs, while improving their ductility. It is generally found that secondary phases enhance the tendency for shear band nucleation and lead to a more homogeneous strain distribution [38–41]. Regarding the interaction of propagating shear bands with precipitates, small precipitates can be avoided (“wrapped”) by shear bands [42], leaving the crystalline phase undeformed [43]. Bigger precipitates block the shear band propagation or co-deform with the glass matrix [42, 43]. These investigations are mostly concerned with smaller volume fractions of crystalline phase, though, and it is unclear if they also apply to nanocrystalline metals.

The purpose of the present work is to study the crossover from glass–crystal nanocomposites to nanocrystals using molecular dynamics (MD) computer simulations. We use the well-established MG $\text{Cu}_{64}\text{Zr}_{36}$ with embedded brittle Laves phase nanocrystallites as a model system. The advantage over studying ductile nanocrystallites is that the

plastic response of the system is exclusively carried by the glassy phase/grain boundaries and thus we can disentangle the grain boundary activity from dislocation activity. As was recently shown [44–46], Laves crystallites can be grown in MD simulations using the Finnis–Sinclair-type potential by Mendeleev [47]. This opens the possibility of growing crystallites in a system of constant composition, thereby obtaining samples ranging from a homogeneous MG, over glass–crystal composites, to nanocrystals.

2. Computational methods and analysis

All MD simulations were performed with Cu–Zr systems using LAMMPS [48] and the Finnis–Sinclair-type potential by Mendeleev *et al.* [47]. The integration time step was 2 fs in all cases.

2.1. Synthesis and annealing procedure

A $\text{Cu}_{64}\text{Zr}_{36}$ metallic glass consisting of $N = 63,108$ atoms was quenched from the melt down to 50 K with a cooling rate of 0.01 K/ps and equilibrated there for 2 ns. This “as-quenched” sample is designated sample I and has dimensions of around $10 \times 10 \times 10 \text{ nm}^3$. In order to facilitate the crystallisation of Cu_2Zr Laves phases [46], we heated the glass to 800 K (which is close to the glass transition T_g [47]) with $\dot{T} = 0.1 \text{ K/ps}$. We held the glass at this temperature for roughly 2 μs and then increased the temperature step-wise to 850 K and then to 900 K to speed up the crystallisation kinetics. Figure 2 shows the complete annealing procedure. Neither a glass transition nor melting were observed; indeed the glass transition temperature

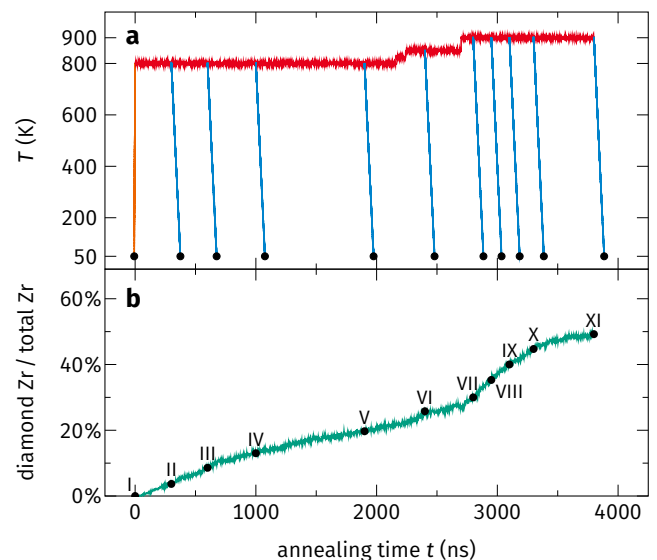


Figure 2: The annealing procedure. (a) Temperature profile. The sample is heated with 0.1 K/ps to 800 K. After around 2 μs the temperature is increased step-wise to increase the crystallisation rate. Snapshots are taken at intervals and cooled down with 0.01 K/ps. (b) The fraction of zirconium atoms in diamond superlattice configurations as a function of annealing time as a rough indicator of crystalline volume fraction. The snapshots are labelled I–XI.

risers with annealing time (see Appendix A). At intermediate steps, snapshots of the simulation were taken and cooled with $\dot{T} = 0.01$ K/ps back to 50 K. These snapshots with different crystalline volume fractions are labelled as sample II–XI. We detected the presence of crystallites and computed the grain sizes as described in Appendix B and found a mix of C14 and C15 Laves phases [49] with an amorphous grain boundary. Details about the nucleation of crystallites are provided in Appendix C.

For later mechanical testing, these samples were replicated $3 \times 1 \times 7$ times to obtain specimen of $30 \times 10 \times 70$ nm³ size. Open boundaries were introduced in x direction to increase the tendency for shear localisation as discussed in Ref. 40. The samples were then equilibrated at target temperatures of 50 K and 250 K for 1 ns. The structural, thermodynamic, and elastic properties were determined using the unreplicated samples with periodic boundaries.

2.2. Artificial nanocrystals by Voronoi construction

As a comparison, we also prepared artificial nanocrystals by choosing a number of random points in a simulation cell, constructing Voronoi cells [50] around those points, and inserting either a C14 or a C15 lattice with random orientation into the cells. This procedure is analogous to the one described in Ref. 51. Assuming spherically shaped grains, we can obtain a given grain diameter d in a simulation cell of volume V using $n = \lfloor 6V/(\pi d^3) \rfloor$ points. We selected approximate grain sizes of 3 nm, corresponding to the grain size in sample XI, as well as 5 nm, 7 nm, 10 nm, and 15 nm, which are closer to the grain sizes obtainable in experiment. The samples were prepared with dimensions similar to the grown crystallite composites and also have open boundaries in x direction. We optimised the resulting structures by molecular statics simulations and equilibrated them at the target temperatures of 50 K and 250 K for 1 ns.

2.3. Relaxation state of the amorphous phase

Metallic glasses exhibit a direct correlation between yield stress and shear modulus G [11], which means that the shear modulus can also serve as an indicator for the relaxation state of the glass. However, the determination of local moduli for grain boundaries is nontrivial, since (1) one needs to measure a localised shear modulus and (2) amorphous metals are anisotropic on the nanometre length scale [52]. We therefore use the Kelvin notation for the stiffness tensor [53], which we calculate per atom as described in Ref. 54. Diagonalisation of this tensor yields five shear moduli [55]. We use the median of the smallest of these, $\langle G_1 \rangle$, as an indicator for the overall shear stiffness of the amorphous phase, assuming that the “softest” shear mode is the one that yields first. More details on the procedure and numerical concerns are discussed in Appendix D.

2.4. Tensile tests

For mechanical testing a constant engineering strain rate of 10^8 s⁻¹ was applied uniaxially in z direction of the

equilibrated samples up to a maximum strain of 12%, which exceeds the yield strain. The deformation was performed for each sample at 50 K and 250 K. Localised deformation was identified using the atomic shear strain η_i [56] as implemented in OVITO [57]. As a measure for the degree of localisation we use the shear localisation parameter $\psi = \sqrt{\sum_{i=1}^N (\eta_i - \bar{\eta})^2 / N}$, with $\bar{\eta} = \sum_{i=1}^N \eta_i / N$, where N is the number of atoms in the system [58].

We define the yield stress σ_y of the samples as the maxi-

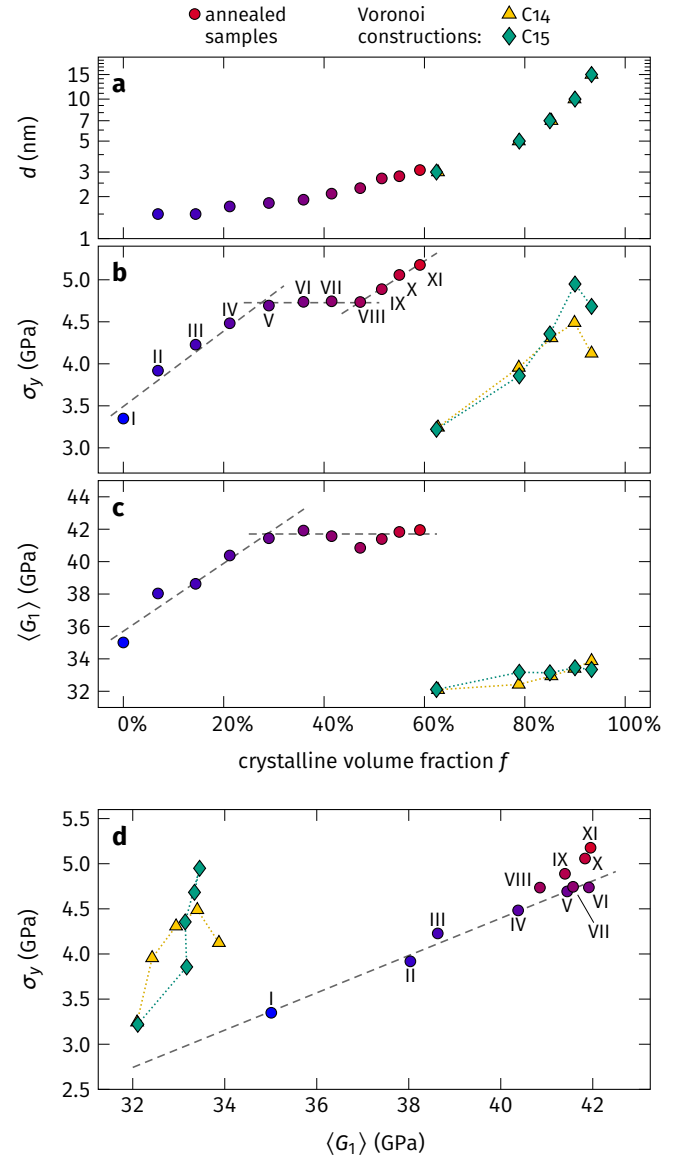


Figure 3: Characterisation of the samples and their mechanical strength. (a) Microstructure as defined by average crystallite diameter d and crystalline volume fraction f . Yield stress at 50 K (b) and median atomic shear modulus $\langle G_1 \rangle$ of the amorphous phase (c) reveal a proportionality $\sigma_y \propto \langle G_1 \rangle$ that breaks down at higher f . This is again illustrated in (d) by plotting both values against each other. The dashed lines serve as a guide for the eye: Samples VIII–XI no longer exhibit the proportionality; neither do the samples created artificially by Voronoi construction. A direct relation to d cannot be observed.

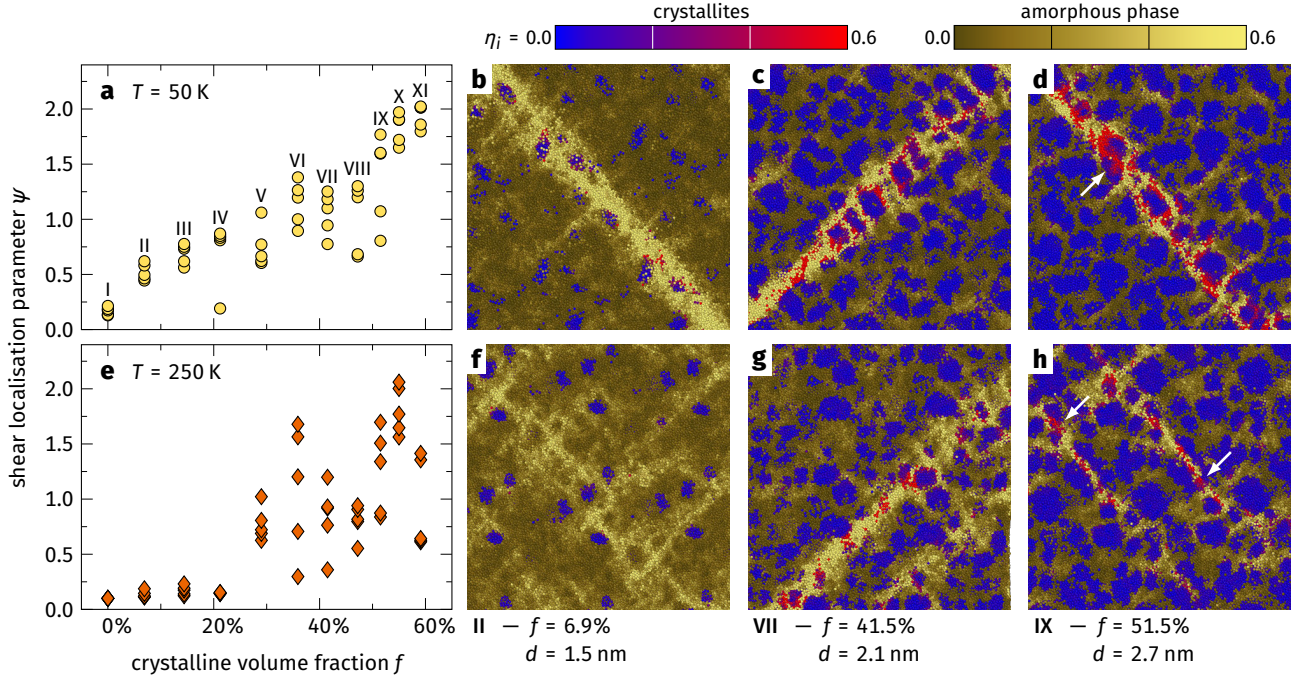


Figure 4: Shear localisation at $\varepsilon = 12\%$ in samples I–XI. The top row shows the results for $T = 50$ K, the bottom row for $T = 250$ K. (a) and (e) show the shear localisation parameter ψ . The snapshots in (b)–(d) and (f)–(h) are coloured according to the atomic shear strain η_i using two different colour maps for the amorphous and the crystalline phase. Crystallites that are cut are marked by arrows. More snapshots are provided in Supplementary Fig. S.5 and S.6.

imum stress in the stress–strain curve. We use this criterion instead of the flow stress, since all phases in the system will soften when damaged. The crystallites are brittle and thus are destroyed when yielding, and the glass undergoes shear softening. Indeed, differently relaxed glasses of the same composition exhibit different maximum stresses but the same flow stress [58, 59].

3. Results

3.1. Mechanical properties and deformation mechanisms

Characterisation of the annealed samples (I–XI) shows that the average crystallite diameters d are quite small (≤ 3 nm) and therefore suitable to explore the sub-10-nm nanocrystalline regime (Fig. 3a). The results of tensile tests at 50 K on these specimen are shown in Fig. 3b. Tests on samples I–XI were repeated five times, but the variation of the yield stress is negligible and the error bars are smaller than the symbols. The results at 250 K are qualitatively similar apart from a uniform decrease of yield strength and are omitted here. They are provided in the Supplementary Fig. S.1. Full stress–strain curves are available in Supplementary Fig. S.2. The general trend is an increase of yield strength σ_y with crystalline volume fraction f . All samples deform by shear banding, except for samples I and II, which exhibit a somewhat more homogeneous deformation at 250 K (see Fig. 4 and Supplementary Figs. S.3 and S.4). We note here that nucleation phenomena at the crystal–glass interface seem to play a minor role for the

strength of the composite, otherwise the differences in yield stresses between 50 K and 250 K would be more complex than a simple offset and depend on the interface area.

According to earlier simulations [42], crystallites with diameters d of around 3 nm should pose no obstacle to shear band propagation and the yield stress should be defined by the amorphous phase alone. The yield stress of the amorphous phase is proportional to its shear modulus G [11]. Figures 3b, 3c, and 3d show that the proportionality between the local shear modulus $\langle G_1 \rangle$ in the grain boundary and the yield stress σ_y works for low volume fractions f : During the annealing process, the amorphous phase relaxes and becomes stiffer. For large volume fractions of the crystalline phase, though, the proportionality with $\langle G_1 \rangle$ breaks down: The glass reaches a maximum stiffness (and therefore a deeply relaxed state), while the yield stress increases further from sample VIII on. At this point the microstructure starts to play a role, since only the crystalline volume fraction f and grain size d continue changing. This also marks the breakdown of the typical mechanisms in glass–crystal composites, where shear bands can always avoid such small crystallites [42].

As a first step towards understanding this transition, we evaluated the strain localisation behaviour of the samples. Figure 4 and Supplementary Figs. S.3 and S.4 show that the shear localisation increases together with the crystalline volume fraction and decreases with temperature. Clearly, STZ activation is a thermally activated process [6] and thus an increased temperature leads to increased

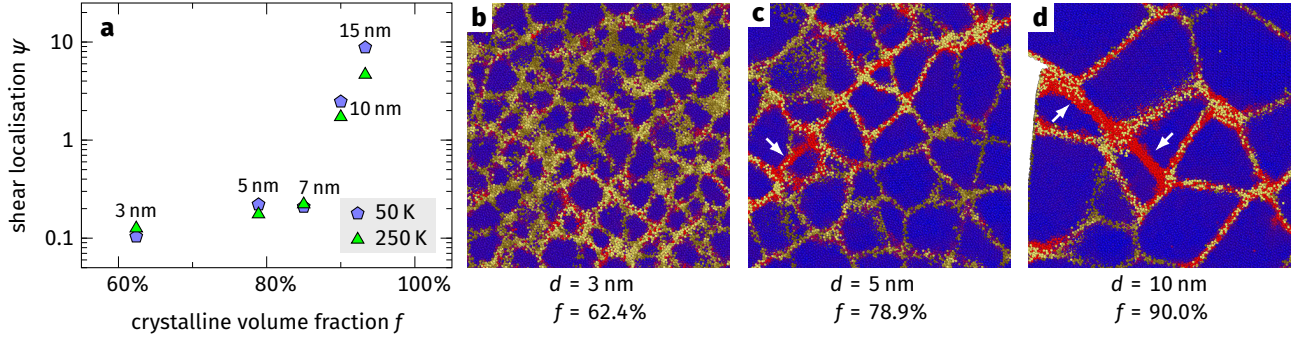


Figure 5: Shear localisation at $\varepsilon = 12\%$ in the samples produced by Voronoi construction. (a) The shear localisation parameter ψ shows that the deformation is rather homogeneous independent of the temperature, indicating that the grain boundary is comparatively weak and plastic events do not require thermal activation. (b)–(d) Snapshots of the atomic shear strain after deformation at 50 K. The colour scale is the same as in Fig. 4. More snapshots are provided in Supplementary Figs. S.5 and S.6.

activation kinetics all over the sample and a more homogeneous deformation. The change of strain localisation with f can be explained by competing mechanisms: The reduction of the amorphous volume fraction leads to a spatial confinement of STZ activation and necessarily increases the heterogeneity of the early deformation stages. This is exacerbated by the increasing heterogeneity of the glassy phase itself: Glasses that are deeply relaxed are defined by a greater difference between liquid-like and solid-like regions, making the deformation once again more heterogeneous [58]. On the other hand, dispersions of small crystallites in a glass matrix were observed to increase the density of shear bands [38]. Therefore, the shear localisation stays low for the samples I–IV at 250 K. Here, the increased temperature enables nucleation of multiple shear bands which is supported by the dispersion of crystallites which serve as shear band nucleation sites [40, 41, 60]. Starting from sample V, the shear bands become more confined and the further growth of the nascent shear bands into mature ones is suppressed. It can be seen in Fig. 4, as well as in Supplementary Figs. S.3 and S.4, that patterns of localised deformation persist in samples with high f , indicating that shear band multiplication still occurs, but that the growth of a multitude of shear bands is suppressed. Consequently, strain localisation is increased. Furthermore, Figs. 4d and 4h show that the confinement additionally leads to the crystallites being cut. Since the crystallites are brittle and stronger than the glass, the yield stress increases, even if the glass phase itself does not harden. Due to the brittleness of the Laves phases, the cut occurs in the form of amorphisation along a favourable lattice plane.

In order to sample more geometries, we also artificially created nanocrystals with 3 nm to 15 nm grain sizes using the Voronoi construction algorithm [51]. We constructed the samples once with the C14 and once with the C15 Laves phase [49], which both occur during the annealing process. We performed the same tensile tests and analyses as for samples I–XI and show the results in Fig. 3. Interestingly, the artificial sample with 3 nm grain size has a drastically reduced strength compared with sample XI, despite their

similar microstructure. Given the previously discussed results, one would expect that the crystallites partake in the deformation and that both samples exhibit the same yield stress. This is not the case. Figure 5b shows that the deformation in the amorphous phase is delocalised and that this homogeneous flow can occur without involvement of the crystalline phase. The reason can be found in Fig. 3c: The grain boundary of the artificially constructed samples is very soft, indicating a high-energy state of the amorphous phase. It is known that this leads to delocalised deformation and lower yield stress [58]. Figure 5b confirms that the grain boundary phase “flows around” the crystallites. With increasing grain size and crystalline volume fraction, though, more and more crystallites are being cut (see Figs. 5c and 5d), despite comparable softness of the grain boundary. This is accompanied by an increase in strain localisation (Fig. 5a). As a result, an inverse Hall–Petch relation (cf. Refs. 5, 12, 61) occurs. The hardening with increasing grain size can be explained by the increasing fraction of crystalline matter that has to deform plastically. Starting with 10 nm grain size, the typical order of magnitude for the breakdown of the Hall–Petch relation [5, 12, 13], shear localisation becomes very high and the yield stress reaches a plateau comparable in magnitude to sample XI. This signifies the transition from a macroscopic plastic response dominated by the grain boundary to a response dominated mainly (although not exclusively) by the grain interior.

3.2. Change of mechanisms as a jamming transition

While shear localisation does not strongly influence the strength of the glass [40], it nevertheless appears to be important for the difference of mechanisms between sample XI and the 3 nm Voronoi construction, as evidenced by Figs. 3, 4, and 5. With increasing f , the contribution of the yield strength of the crystallites increases, finally exceeding the strength of the grain boundary. As illustrated in Fig. 6, this behaviour can be understood as a kind of jamming transition, which is known from granular matter [62–64]: At lower packing density ϕ , the granular particles can flow freely. In our analogy, this means that the shear band can

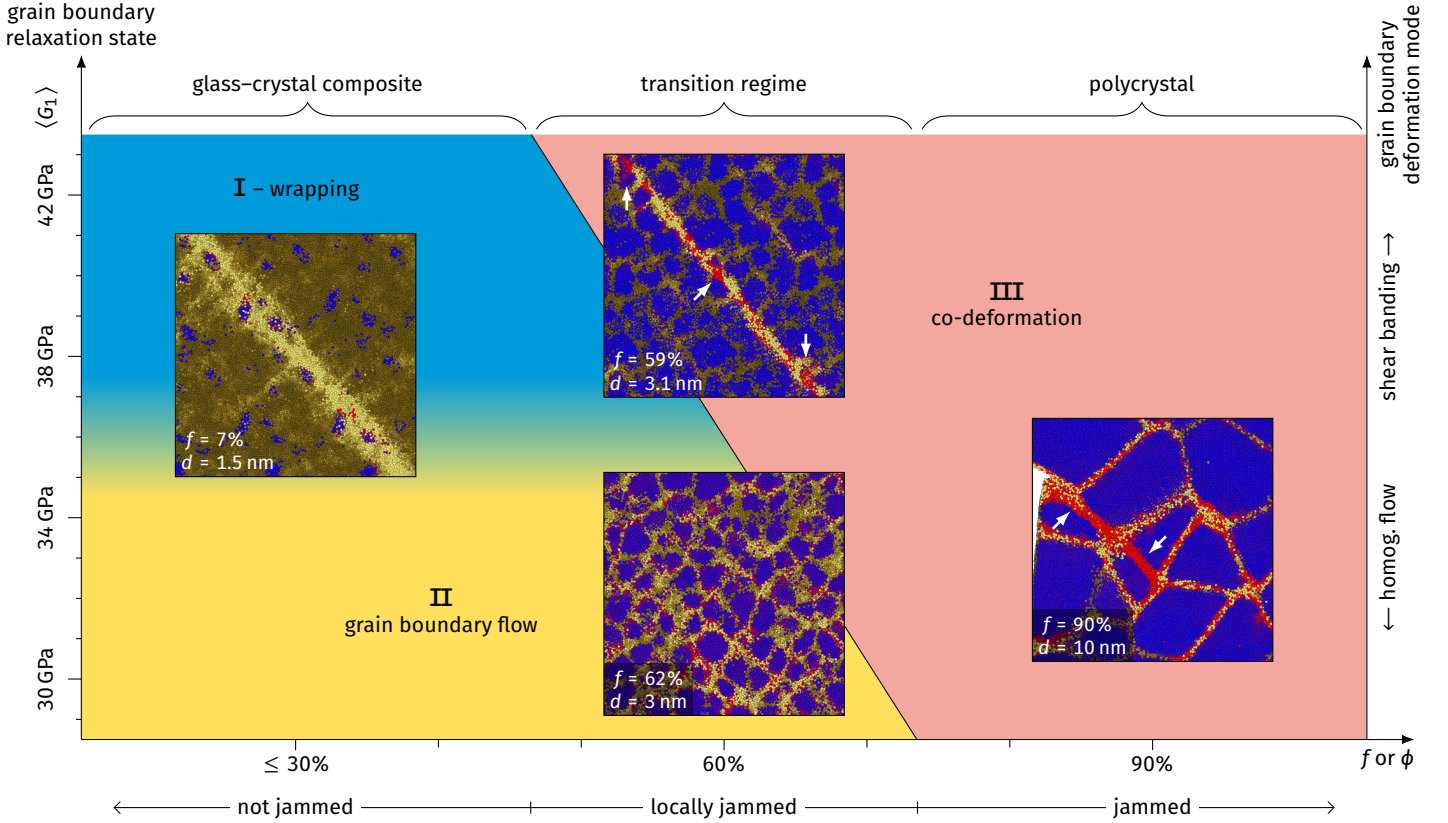


Figure 6: Mechanism map of the crossover from glassy to crystalline plasticity as a jamming-like transition. For small crystalline volume fractions f , the plastic response depends only on the amorphous phase. Depending on its relaxation state (quantified by its local shear modulus $\langle G_1 \rangle$), we distinguish two regimes: (I) The formation of a single shear band that can avoid the crystallites by “wrapping” around them and (II) a homogeneous flow of the glassy phase. The distinction is solely controlled by the relaxation state of the amorphous phase, be it bulk glass or grain boundary. With increasing crystalline volume fraction f (and thereby increasing packing density ϕ of the crystallites), clusters of crystallites become locally jammed. While the homogeneously flowing grain boundary can deform while avoiding these areas, the localised shear band can only propagate by cutting through the crystallites. Therefore, the onset of regime III, i.e., the co-deformation of both phases, also depends on the state of the grain boundary. Finally, a further increase of f leads to full jamming and co-deformation independent of the grain boundary state. This is the usual scenario in nanocrystals with grain sizes above roughly 10 nm and in coarse-grained polycrystals.

wrap around crystallites and that homogeneous flow around the crystallites is possible. When increasing ϕ —which is roughly equivalent to f in our case—we locally get a few clusters of jammed crystallites. In the case of localised deformation, the shear band samples only a small volume. This volume itself is jammed and thus the crystallites either need to be cut, or a new shear band nucleated. The latter case probably costs more energy and there is already a stress concentration at the shear band front. This does not concern the homogeneously flowing grain boundary, though, because a local jam in one area can be avoided by flowing somewhere else. In terms of jamming, this corresponds to keeping the number of contacts constant, but increasing the system size, thereby unjamming the system [65, 66]. The final state is a completely jammed system, which corresponds to the classical picture of a polycrystal: Here, the crystallites always carry a large part of the plasticity (i.e., they need to be “cut”) independent of the grain boundary state. In our system, no Hall–Petch effect can be observed due to the brittleness of the Laves phases and the yield stress reaches a maximum.

The classical picture of the jamming transition corresponds more closely to completely homogeneous flow of the grain boundary. For hard spheres, a critical packing density of around $\phi = 64\%$ is often found [63, 64]. Looking at Fig. 3, we find that this roughly corresponds to the critical f for cutting crystallites, which lies somewhere between the 3 nm and 5 nm samples. This is remarkable, since the assumptions of the hard sphere model barely hold in our system. Nonetheless, the model appears to apply at least approximately. We can also see that the different yield stresses of the C14 and the C15 phase only come into play for large f ; before that point the strength of the sample is still grain-boundary dominated. We note that the volume fraction f is independent of any length scale. The length scale gets reintroduced by the thickness of the grain boundaries, which controls f for densely packed crystallites of a given diameter. For typical grain boundary widths in the nanometre range, the jamming transition occurs somewhere below a grain size of 10 nm.

The possibility of purely grain-boundary-mediated deformation has been reported before for Ni [67], where it is

enabled by a free percolation path for shear bands through the sample. Our results furthermore indicate that the participation of the crystalline phase in the deformation also depends on the intrinsic proclivity towards strain localisation in the amorphous phase. Pure metals in simulations at nanometre-scale grain sizes always have an unrelaxed grain boundary, since massive grain growth would set in on relaxation or annealing. The softening with decreasing grain sizes below 10 nm that has been found before [68] is thus analogous to our Voronoi constructed samples: For grain sizes increasing from 3 nm to 10 nm, the number of crystallites participating in the deformation rises, and with it the yield stress. The only difference is that the brittle failure of the crystallites is replaced by plastic flow. We confirmed the transferability of our observation to ductile metals with example simulations of nanocrystalline copper using the potential by Mishin *et al.* [69] (see Supplementary Fig. S.7).

A maximum strength should be obtained when the grain boundary is very relaxed and the deformation is localised, but when the grains are small enough to suppress dislocation nucleation. Recent experimental results on Mg-based nanocrystals in the form of a brittle Laves phase with a large fraction of amorphous grain boundary confirm the existence of such a regime [70]: Shear-band-like deformation occurs and cuts through the crystallites. The strength of the material is very high compared to Mg-based polycrystals and glasses.

3.3. Strengthening through grain boundary relaxation

Finally, since the mechanical properties of very fine-grained nanocrystals depend largely on the properties of the amorphous phase, it should be possible to modify the properties of the artificially created sample with C15 phase and grain size 3 nm by an annealing procedure. We annealed the sample at 900 K for 4 ns. No grain growth was observed. Afterwards, we equilibrated the sample at 50 K and performed a tensile test with the same parameters as before. Figure 7 shows that the structure now almost resembles sample XI in its behaviour. The deformation is localised and the strength is increased.

Repeating the procedure with the sample with grain size 7 nm, we find that the yield strength at 50 K increases to around 5.1 GPa. Again, no grain growth was observable. This number is comparable with the yield strength of sample XI and the sample with 10 nm grain size. Consequently, we conclude that an inverse Hall–Petch effect is only found when the grain boundary is in a rather unrelaxed state and deforms more homogeneously. In that case, the strength of the material depends on the fraction of amorphous boundary phase. Note that the samples I–X are less strong than XI, but are not true nanocrystals due to the large amorphous volume fraction.

Experiments show that annealing treatments of nanocrystalline metals lead to grain boundary relaxation and strengthening, and for grain sizes smaller than 10 nm an

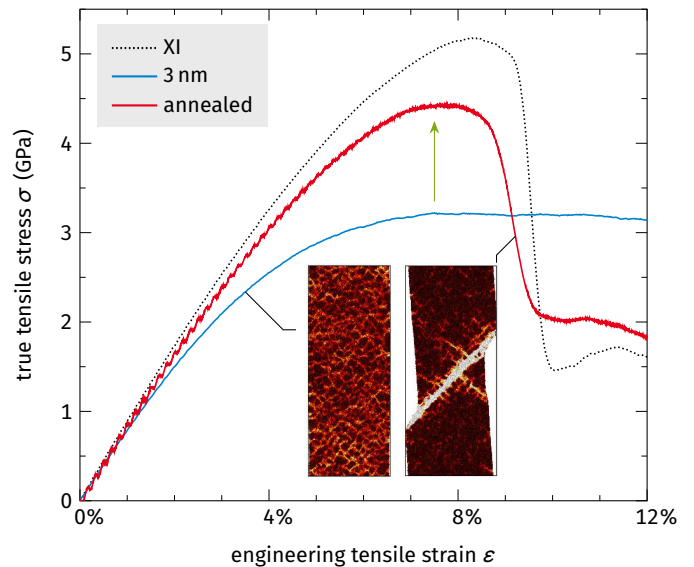


Figure 7: Effect of an annealing treatment on a Voronoi construction with C15 crystalline phase and 3 nm grain size. While the untreated sample deforms homogeneously, the annealed sample localises the shear strain. This results in increased strength and brittleness. The stress–strain curve for sample XI, which has a comparable microstructure, is shown for comparison.

increased strain localisation was found [71]. This is consistent with the current observations and with a glass-like behaviour of the grain boundary. As stated earlier, the strain localisation and strength in metallic glasses depend on the relaxation state. As such, the strengthening observed in our simulations provides further evidence for STZ-like mechanisms in the grain boundary.

4. Conclusion

In our MD simulations on $\text{Cu}_{64}\text{Zr}_{36}$ glass samples with different volume fractions of brittle Laves phases, we find that the grain boundary phase behaves like a metallic glass under constraint from the abutting crystallites. The switch from glass-like to grain-boundary-mediated plasticity depends on the crystalline volume fraction and the grain boundary state. Tensile test simulations reveal three regimes: (1) For low crystalline volume fractions, the system behaves like a glass–crystal composite with small crystallites [42], i.e., plastic flow is localised in the amorphous phase. (2) With increasing crystalline volume fraction, clusters of crystallites can become jammed. The behaviour of such a system depends critically on the grain boundary relaxation state, which governs the strain localisation tendencies in the amorphous phase: If the flow is homogeneous, jammed clusters can be avoided and the deformation stays confined to the grain boundary. If these clusters become larger, they nevertheless contribute partially to the material strength, as would be expected from a simple composite model. If the flow is instead localised in a shear band, the jammed clusters present obstacles to the deformation and need to be cut. Thus, they contribute fully to the strength

of the material. (3) At more typical experimental grain sizes ≥ 10 nm, the system is jammed completely and the grain boundary can no longer be the sole carrier of plasticity, leading to co-deformation. In this typical polycrystalline regime, the Hall–Petch scaling becomes valid. These observations are transferable to ductile metals, although the “cutting” of the brittle crystallites is replaced by dislocation activity inside the grains, and the transition regime is most likely less sharp. Regarding the experimental observations of an inverse Hall–Petch effect, we conclude that even polycrystals with very small grain sizes only soften under specific conditions, namely when the deformation is delocalised and grain-boundary dominated. Therefore, experiments conducted at different grain sizes and with different grain boundary compositions are not directly comparable.

Acknowledgements

Financial support by the Deutsche Forschungsgemeinschaft (DFG) through project grant no. AL 578/6-2 is gratefully acknowledged. Calculations for this research were conducted on the Lichtenberg high performance computer of the Technische Universität Darmstadt.

Appendix A. Change of glass transition temperature with annealing

We evaluated the change of glass transition temperature T_g of the samples I–XI by reheating them from 50 K to 1500 K with $\dot{T} = 0.1$ K/ps. The resulting potential energy over temperature plot is shown in Fig. A.8. An upper bound for the glass transition temperature is indicated by

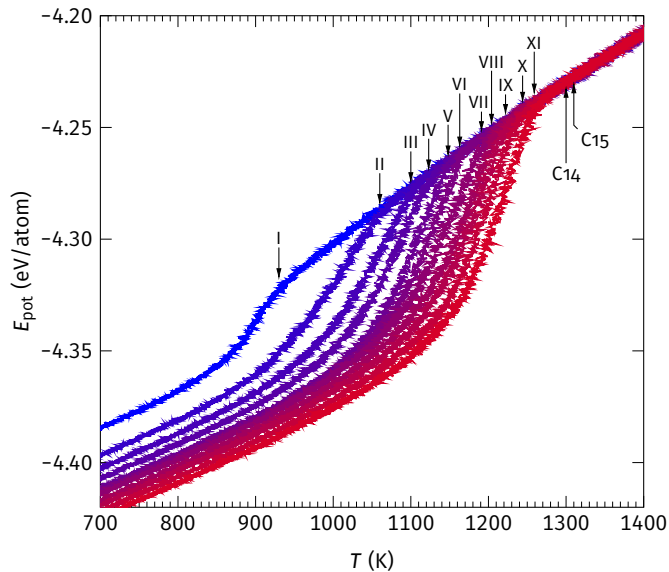


Figure A.8: Change of glass transition temperature with annealing. Arrows indicate the upper bound for T_g for the different samples, as well as an estimate for the melting points of the C14 and C15 Laves phases.

arrows. Additionally, the melting points of the C14/C15 Laves phases are indicated in the plot. These were estimated by relaxing a liquid/crystal interface at different temperatures. The transition temperature for the samples continually rises with annealing time and no second melting point for the contained crystallites can be observed. This indicates that the liquefaction process for both phases occurs simultaneously. The reason is most likely the small size of the crystallites.

Appendix B. Detection and analysis of the crystalline phase

The software package OVITO [57] was used for all analyses. Basic structural analysis was performed using Voronoi tessellation, which divides the simulation cell into one polyhedron around each atom [50, 72]. The polyhedra are characterised by the Voronoi index $\langle n_3, n_4, n_5, n_6 \rangle$, where n_i denotes the number of i -edged faces of the polyhedron. There exists no ready-made detection algorithm for Laves phases. In lieu thereof, we used the following method: The zirconium atoms in the Laves phases are characterised by a hexagonal (C14) or cubic (C15) diamond superstructure [49]. Thus, they were identified by applying a diamond structure identification algorithm [73]. The copper atoms in both Laves phases appear as Voronoi $\langle 0, 0, 12, 0 \rangle$ icosahedra [49]. Thus, those atoms that are either in a zirconium diamond superstructure or that are copper icosahedra neighbouring such zirconium atoms, were identified as belonging to a Laves phase. We find that crystallisation occurs almost immediately upon annealing, reaching a saturation after roughly $4 \mu\text{s}$ (see Fig. 2). The crystallites are a mix of C14 and C15 Laves phases, which have very similar cohesive energies in the potential we used (-4.496 eV/atom for

Table B.1: Properties of the composites. For each sample, the crystalline volume fraction f , the average grain size d , the number density ρ_n , and the potential energy E_{pot} of the whole system at 0 K is listed. Note that the average potential energy is partly lower than for the pure Laves phases (-4.496 eV/atom for C14 and -4.497 eV/atom for C15). This is due to the different composition ($\text{Cu}_{64}\text{Zr}_{36}$ vs. Cu_2Zr), not due to the occurrence of a different phase.

Sample	f (%)	d (nm)	ρ_n (nm^{-3})	E_{pot} (eV/atom)
I	0.0		63.15	-4.483
II	6.9	1.5	63.27	-4.495
III	14.4	1.5	63.33	-4.500
IV	21.2	1.7	63.37	-4.505
V	29.0	1.8	63.42	-4.509
VI	35.9	1.9	63.43	-4.510
VII	41.5	2.1	63.44	-4.512
VIII	47.2	2.3	63.47	-4.515
IX	51.5	2.7	63.48	-4.517
X	55.0	2.8	63.50	-4.519
XI	59.1	3.1	63.53	-4.522

C14 and -4.497 eV/atom for C15). The structural motifs of the Laves phases—copper-centred icosahedra and Zr-centred $\langle 0, 0, 12, 4 \rangle$ (or “Z16”) polyhedra [49]—also appear as low-energy configurations in the glass [74, 75]. The grain boundary stays amorphous in all samples.

In order to obtain an approximation for the grain sizes in the annealed samples, we assumed that all crystallites are spherical and equal in size. The grain size d is then

$$d = \sqrt[3]{\frac{6fN\Omega_{\text{Laves}}}{\pi n}}, \quad (\text{B.1})$$

where f is the crystalline volume fraction, N the number of atoms in the system, Ω_{Laves} the average atomic volume in the Laves phase ($\approx 15.31 \text{ \AA}^3$), and n the number of crystallites obtained by cluster analysis. A detailed listing of the samples’ properties can be found in Table B.1.

Appendix C. Nucleation of the crystallites

Figure C.9 shows the crystallisation process. We can see that the formation of the full crystalline phase is preceded by the agglomeration of ordered clusters. This means that crystallisation starts preferentially in the most ordered regions of the glass. The reason is of course the structural similarity: Nelson postulated some time ago that Frank–Kasper polyhedra, such as the copper-centred icosahedra and the zirconium-centred Z16 polyhedra, play an important structural role in metallic glasses and speculated that the ideal glass may be a Frank–Kasper phase with infinite unit cell [76, 77]. Therefore, the Laves phases arise most naturally in the most ordered regions of the glass.

Appendix D. Analysis of the elastic properties

The per-atom shear moduli were calculated as described in Ref. 54: Different stress states were applied at 0 K and the stiffness tensor calculated with Hooke’s law from the strain response for every atom using OVITO’s atomic strain analysis [57]. Diagonalisation of this tensor yields five shear moduli [55]. Their distributions are plotted exemplarily for three systems in Fig. D.10. The insets reveal that negative moduli occur (as expected for amorphous systems, see Ref. 55), which decrease in number the more the glass is relaxed. In order to extract a single number that most closely relates to the mechanical strength of the phase, we decided on an average of the lowest modulus, G_1 . Because of large negative outliers, the arithmetic mean is not representative (e.g., it would be -32 GPa for sample I). Instead, we used the median.

We also note that the line in Fig. 3d does not pass through the graph’s origin as expected from experimental data [11]. Essentially, $\langle G_1 \rangle$ does not correspond to a macroscopic shear modulus. We know that a system becomes mechanically unstable if a certain fraction of atoms has negative moduli [78–80], although a certain number can be accommodated by the surrounding matrix [55]. Thus, $\langle G_1 \rangle$

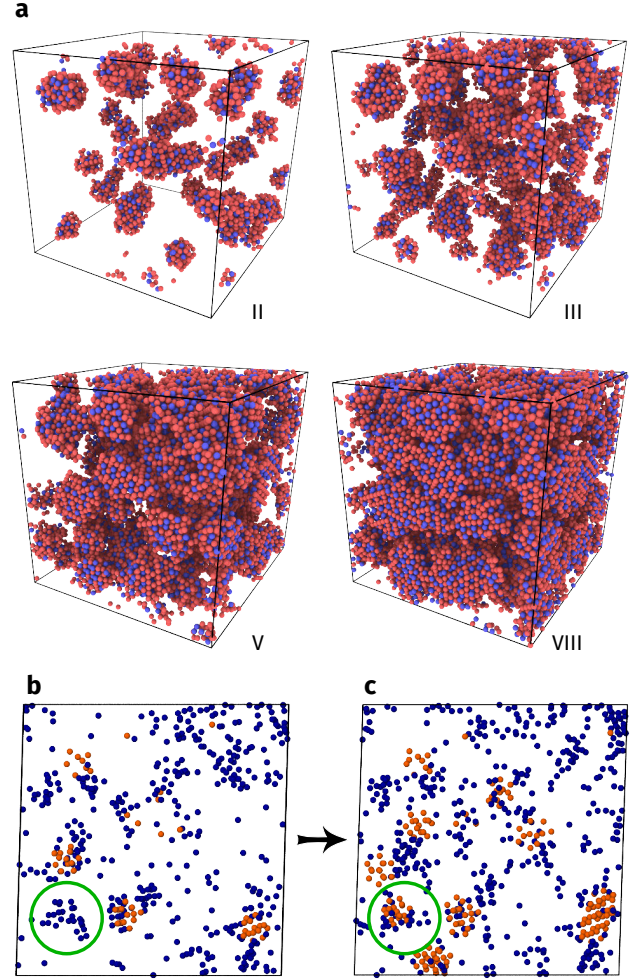


Figure C.9: Snapshots of the crystallisation process. (a) Four exemplary snapshots of samples with different crystalline volume fraction. Only atoms identified as belonging to a Laves phase are rendered. (b)–(c) Slices through the sample after 200 ns (b) and 300 ns (c) annealing time are shown. The latter corresponds to sample II. All atoms except zirconium in Z16 configuration were deleted for the visualisation. Orange atoms belong to a diamond superlattice, while blue atoms are located in amorphous regions. The green circle indicates that crystallisation occurs preferentially in regions that already exhibit ordering tendencies.

is not necessarily zero if the critical fraction is surpassed and the yield stress becomes zero.

Appendix E. Supplementary data

Supplementary data accompanies this article.

References

- [1] J. Lohmiller, M. Grewer, C. Braun, A. Kobler, C. Kübel, K. Schüller, V. Honkimäki, H. Hahn, O. Kraft, R. Birringer, P. A. Gruber, Untangling dislocation and grain boundary mediated plasticity in nanocrystalline nickel, *Acta Mater.* 65 (2014) 295–307. doi:10.1016/j.actamat.2013.10.071.
- [2] H. Gleiter, Nanocrystalline materials, *Prog. Mater Sci.* 33 (1989) 223–315. doi:10.1016/0079-6425(89)90001-7.

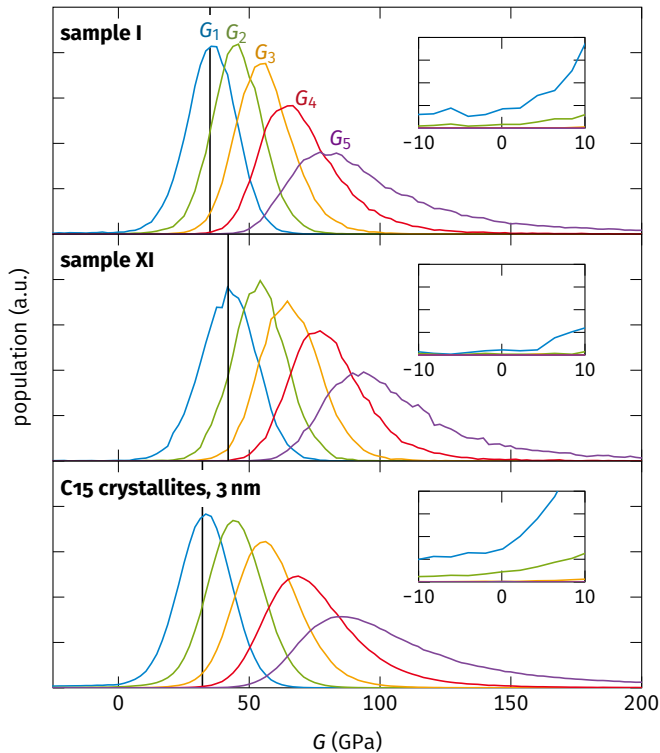


Figure D.10: Histograms for the per-atom shear moduli G_1 to G_5 for selected samples. Only atoms in the amorphous phase are included. The vertical lines represent the median $\langle G_1 \rangle$. The insets show that negative shear moduli occur, especially for the less relaxed glasses. Scaling of the ordinate axis is the same for all three cases.

- [3] M. A. Meyers, A. Mishra, D. J. Benson, Mechanical properties of nanocrystalline materials, *Prog. Mater. Sci.* 51 (2006) 427–556. doi:10.1016/j.pmatsci.2005.08.003.
- [4] D. Wolf, V. Yamakov, S. R. Phillpot, A. Mukherjee, H. Gleiter, Deformation of nanocrystalline materials by molecular-dynamics simulation: relationship to experiments?, *Acta Mater.* 53 (2005) 1–40. doi:10.1016/j.actamat.2004.08.045.
- [5] J. R. Trelewicz, C. A. Schuh, The Hall–Petch breakdown in nanocrystalline metals: A crossover to glass-like deformation, *Acta Mater.* 55 (2007) 5948–5958. doi:10.1016/j.actamat.2007.07.020.
- [6] A. Argon, Plastic deformation in metallic glasses, *Acta Metall.* 27 (1979) 47–58. doi:http://dx.doi.org/10.1016/0001-6160(79)90055-5.
- [7] M. L. Falk, J. S. Langer, Dynamics of viscoplastic deformation in amorphous solids, *Phys. Rev. E* 57 (1998) 7192–7205. doi:10.1103/PhysRevE.57.7192.
- [8] A. C. Lund, T. G. Nieh, C. A. Schuh, Tension/compression strength asymmetry in a simulated nanocrystalline metal, *Phys. Rev. B* 69 (2004) 012101. doi:10.1103/PhysRevB.69.012101.
- [9] A. S. Argon, S. Yip, The strongest size, *Philos. Mag. Lett.* 86 (2006) 713–720. doi:10.1080/09500830600986091.
- [10] M. Grewer, R. Birringer, Shear shuffling governs plastic flow in nanocrystalline metals: An analysis of thermal activation parameters, *Phys. Rev. B* 89 (2014) 184108. doi:10.1103/PhysRevB.89.184108.
- [11] W. L. Johnson, K. Samwer, A universal criterion for plastic yielding of metallic glasses with a $(t/T_g)^{2/3}$ temperature dependence, *Phys. Rev. Lett.* 95 (2005) 195501. doi:10.1103/PhysRevLett.95.195501.
- [12] C. A. Schuh, T. G. Nieh, H. Iwasaki, The effect of solid solution W additions on the mechanical properties of nanocrystalline Ni, *Acta Mater.* 51 (2003) 431–443. doi:10.1016/S1359-6454(02)00427-5.
- [13] A. J. Detor, C. A. Schuh, Tailoring and patterning the grain size of nanocrystalline alloys, *Acta Mater.* 55 (2007) 371–379. doi:10.1016/j.actamat.2006.08.032.
- [14] D. Wolf, J. Wang, S. R. Phillpot, H. Gleiter, On the thermodynamic relationship between nanocrystalline materials and glasses, *Phys. Lett. A* 205 (1995) 274–280. doi:10.1016/0375-9601(95)00545-E.
- [15] G.-P. Zheng, M. Li, Crystal instability in nanocrystalline materials, *Acta Mater.* 55 (2007) 5464–5472. doi:10.1016/j.actamat.2007.06.013.
- [16] T. Brink, D. Şopu, K. Albe, Solid-state amorphization of Cu nanolayers embedded in a $\text{Cu}_{64}\text{Zr}_{36}$ glass, *Phys. Rev. B* 91 (2015) 184103. doi:10.1103/PhysRevB.91.184103.
- [17] S.-J. Zhao, K. Albe, H. Hahn, Grain size dependence of the bulk modulus of nanocrystalline nickel, *Scr. Mater.* 55 (2006) 473–476. doi:10.1016/j.scriptamat.2006.04.043.
- [18] M. Grewer, J. Markmann, R. Karos, W. Arnold, R. Birringer, Shear softening of grain boundaries in nanocrystalline Pd, *Acta Mater.* 59 (2011) 1523–1529. doi:10.1016/j.actamat.2010.11.016.
- [19] W. Dmowski, T. Iwashita, C.-P. Chuang, J. Almer, T. Egami, Elastic heterogeneity in metallic glasses, *Phys. Rev. Lett.* 105 (2010) 205502. doi:10.1103/PhysRevLett.105.205502.
- [20] J. Ding, Y. Q. Cheng, E. Ma, Correlating local structure with inhomogeneous elastic deformation in a metallic glass, *Appl. Phys. Lett.* 101 (2012) 121917. doi:10.1063/1.4754121.
- [21] J. Ding, Y. Q. Cheng, E. Ma, Quantitative measure of local solidity/liquidity in metallic glasses, *Acta Mater.* 61 (2013) 4474–4480. doi:10.1016/j.actamat.2013.04.016.
- [22] J. Ding, S. Patinet, M. L. Falk, Y. Cheng, E. Ma, Soft spots and their structural signature in a metallic glass, *Proceedings of the National Academy of Sciences* 111 (2014) 14052–14056. doi:10.1073/pnas.1412095111.
- [23] J. Weissmüller, J. Löffler, M. Kleber, Atomic structure of nanocrystalline metals studied by diffraction techniques and EXAFS, *Nanostruct. Mater.* 6 (1995) 105–114. doi:10.1016/0965-9773(95)00034-8.
- [24] M. Ames, J. Markmann, R. Karos, A. Michels, A. Tschöpe, R. Birringer, Unraveling the nature of room temperature grain growth in nanocrystalline materials, *Acta Mater.* 56 (2008) 4255–4266. doi:10.1016/j.actamat.2008.04.051.
- [25] J. Weissmüller, Alloy effects in nanostructures, *Nanostruct. Mater.* 3 (1993) 261–272. doi:10.1016/0965-9773(93)90088-S.
- [26] R. Kirchheim, Grain coarsening inhibited by solute segregation, *Acta Mater.* 50 (2002) 413–419. doi:10.1016/S1359-6454(01)00338-X.
- [27] F. Liu, R. Kirchheim, Nano-scale grain growth inhibited by reducing grain boundary energy through solute segregation, *J. Cryst. Growth* 264 (2004) 385–391. doi:10.1016/j.jcrysgro.2003.12.021.
- [28] D. L. Beke, C. Cserháti, I. A. Szabó, Segregation inhibited grain coarsening in nanocrystalline alloys, *J. Appl. Phys.* 95 (2004) 4996–5001. doi:10.1063/1.1688461.
- [29] C. E. Krill, III, H. Ehrhardt, R. Birringer, Thermodynamic stabilization of nanocrystallinity, *Z. Metallk.* 96 (2005) 1134–1141. doi:10.3139/146.101152.
- [30] J. Schäfer, Y. Ashkenazy, K. Albe, R. S. Averback, Effect of solute segregation on thermal creep in dilute nanocrystalline Cu alloys, *Mater. Sci. Eng. A* 546 (2012) 307–313. doi:10.1016/j.msea.2012.03.078.
- [31] L. Kurmanava, Y. Ivanisenko, J. Markmann, K. Yang, H.-J. Fecht, J. Weissmüller, Work hardening and inherent plastic instability of nanocrystalline metals, *Phys. Status Solidi RRL* 4 (2010) 130–132. doi:10.1002/pssr.201004095.
- [32] J. Schäfer, A. Stukowski, K. Albe, Plastic deformation of nanocrystalline Pd–Au alloys: On the interplay of grain boundary solute segregation, fault energies and grain size, *Acta Mater.* 59 (2011) 2957–2968. doi:10.1016/j.actamat.2011.01.036.
- [33] D. Udler, D. N. Seidman, Solute-atom segregation at symmetrical twist boundaries studied by Monte Carlo simulation, *Phys. Sta-*

- tus Solidi B 172 (1992) 267–286. doi:10.1002/pssb.2221720124.
- [34] T. J. Rupert, J. C. Trenkle, C. A. Schuh, Enhanced solid solution effects on the strength of nanocrystalline alloys, *Acta Mater.* 59 (2011) 1619–1631. doi:10.1016/j.actamat.2010.11.026.
- [35] J. Schäfer, K. Albe, Competing deformation mechanisms in nanocrystalline metals and alloys: Coupled motion versus grain boundary sliding, *Acta Mater.* 60 (2012) 6076–6085. doi:10.1016/j.actamat.2012.07.044.
- [36] J. Schäfer, K. Albe, Influence of solutes on the competition between mesoscopic grain boundary sliding and coupled grain boundary motion, *Scr. Mater.* 66 (2012) 315–317. doi:10.1016/j.scriptamat.2011.11.031.
- [37] S. Özerinç, K. Tai, N. Q. Vo, P. Bellon, R. S. Averbach, W. P. King, Grain boundary doping strengthens nanocrystalline copper alloys, *Scr. Mater.* 67 (2012) 720–723. doi:10.1016/j.scriptamat.2012.06.031.
- [38] K. Hajlaoui, A. R. Yavari, A. LeMoulec, W. J. Botta, F. G. Vaughan, J. Das, A. L. Greer, A. Kvick, Plasticity induced by nanoparticle dispersions in bulk metallic glasses, *J. Non-Cryst. Solids* 353 (2007) 327–331. doi:10.1016/j.jnoncrysol.2006.10.011.
- [39] D. C. Hofmann, J.-Y. Suh, A. Wiest, G. Duan, M.-L. Lind, M. D. Demetriou, W. L. Johnson, Designing metallic glass matrix composites with high toughness and tensile ductility, *Nature* 451 (2008) 1085–1089. doi:10.1038/nature06598.
- [40] K. Albe, Y. Ritter, D. Şopu, Enhancing the plasticity of metallic glasses: Shear band formation, nanocomposites and nanoglasses investigated by molecular dynamics simulations, *Mech. Mater.* 67 (2013) 94–103. doi:10.1016/j.mechmat.2013.06.004.
- [41] A. Zaheri, F. Abdeljawad, M. Haataja, Simulation study of mechanical properties of bulk metallic glass systems: martensitic inclusions and twinned precipitates, *Model. Simul. Mater. Sci. Eng.* 22 (2014) 085008. doi:10.1088/0965-0393/22/8/085008.
- [42] T. Brink, M. Peterlechner, H. Rösner, K. Albe, G. Wilde, Influence of crystalline nanoprecipitates on shear-band propagation in Cu–Zr-based metallic glasses, *Phys. Rev. Appl.* 5 (2016) 054005. doi:10.1103/PhysRevApplied.5.054005.
- [43] S. Pauly, G. Liu, S. Gorantla, G. Wang, U. Kühn, D. Kim, J. Eckert, Criteria for tensile plasticity in Cu–Zr–Al bulk metallic glasses, *Acta Mater.* 58 (2010) 4883–4890. doi:10.1016/j.actamat.2010.05.026.
- [44] C. Tang, P. Harrowell, Predicting the solid state phase diagram for glass-forming alloys of copper and zirconium, *J. Phys.: Condens. Matter* 24 (2012) 245102. doi:10.1088/0953-8984/24/24/245102.
- [45] J. Zemp, M. Celino, B. Schönfeld, J. F. Löffler, Icosahedral superclusters in Cu₆₄Zr₃₆ metallic glass, *Phys. Rev. B* 90 (2014) 144108. doi:10.1103/PhysRevB.90.144108.
- [46] J. Zemp, M. Celino, B. Schönfeld, J. F. Löffler, Crystal-like rearrangements of icosahedra in simulated copper-zirconium metallic glasses and their effect on mechanical properties, *Phys. Rev. Lett.* 115 (2015) 165501. doi:10.1103/PhysRevLett.115.165501.
- [47] M. I. Mendelev, M. J. Kramer, R. T. Ott, D. J. Sordelet, D. Yagodin, P. Popel, Development of suitable interatomic potentials for simulation of liquid and amorphous Cu–Zr alloys, *Philos. Mag.* 89 (2009) 967–987. doi:10.1080/14786430902832773.
- [48] S. Plimpton, Fast parallel algorithms for short-range molecular dynamics, *J. Comp. Phys.* 117 (1995) 1–19, <http://lammps.sandia.gov/>. doi:10.1006/jcph.1995.1039.
- [49] M. De Graef, M. E. McHenry, *Structure of Materials: An Introduction to Crystallography, Diffraction, and Symmetry*, Cambridge University Press, 2007.
- [50] G. Voronoï, Nouvelles applications des paramètres continus à la théorie des formes quadratiques, *J. Reine Angew. Math.* 134 (1908) 198–287. doi:10.1515/crll.1908.134.198.
- [51] P. M. Derlet, H. Van Swygenhoven, Atomic positional disorder in fcc metal nanocrystalline grain boundaries, *Phys. Rev. B* 67 (2003) 014202. doi:10.1103/PhysRevB.67.014202.
- [52] Y. Luo, Q.-K. Li, M. Li, Mechanical anisotropy at the nanoscale in amorphous solids, *J. Appl. Phys.* 117 (2015) 044301. doi:10.1063/1.4906408.
- [53] W. Thomson, Elements of a mathematical theory of elasticity, *Philos. Trans. Roy. Soc. London* 146 (1856) 481–498. doi:10.1098/rstl.1856.0022.
- [54] T. Brink, L. Koch, K. Albe, Structural origins of the boson peak in metals: From high-entropy alloys to metallic glasses, *Phys. Rev. B* 94 (2016) 224203. doi:10.1103/PhysRevB.94.224203.
- [55] P. M. Derlet, R. Maaß, J. F. Löffler, The boson peak of model glass systems and its relation to atomic structure, *Eur. Phys. J. B* 85 (2012) 148. doi:10.1140/epjb/e2012-20902-0.
- [56] F. Shimizu, S. Ogata, J. Li, Theory of shear banding in metallic glasses and molecular dynamics calculations, *Mater. Trans.* 48 (2007) 2923–2927. doi:10.2320/matertrans.MJ200769.
- [57] A. Stukowski, Visualization and analysis of atomistic simulation data with OVITO – the Open Visualization Tool, *Model. Simul. Mater. Sci.* 18 (2010) 015012, <http://ovito.org/>. doi:10.1088/0965-0393/18/1/015012.
- [58] Y. Q. Cheng, A. J. Cao, E. Ma, Correlation between the elastic modulus and the intrinsic plastic behavior of metallic glasses: The roles of atomic configuration and alloy composition, *Acta Mater.* 57 (2009) 3253–3267. doi:10.1016/j.actamat.2009.03.027.
- [59] Y. Cheng, A. Cao, H. Sheng, E. Ma, Local order influences initiation of plastic flow in metallic glass: Effects of alloy composition and sample cooling history, *Acta Mater.* 56 (2008) 5263–5275. doi:10.1016/j.actamat.2008.07.011.
- [60] Y. S. Wang, G. J. Hao, Y. Zhang, J. P. Lin, L. Song, J. W. Qiao, The role of the interface in a Ti-based metallic glass matrix composite with in situ dendrite reinforcement, *Surf. Interface Anal.* 46 (2014) 293–296. doi:10.1002/sia.5413.
- [61] K. J. Van Vliet, S. Tsikata, S. Suresh, Model experiments for direct visualization of grain boundary deformation in nanocrystalline metals, *Appl. Phys. Lett.* 83 (2003) 1441–1443. doi:10.1063/1.1597417.
- [62] M. E. Cates, J. P. Wittmer, J.-P. Bouchaud, P. Claudin, Jamming, force chains, and fragile matter, *Phys. Rev. Lett.* 81 (1998) 1841–1844. doi:10.1103/PhysRevLett.81.1841.
- [63] A. J. Liu, S. R. Nagel, The jamming transition and the marginally jammed solid, *Annu. Rev. Condens. Matter Phys.* 1 (2010) 347–369. doi:10.1146/annurev-conmatphys-070909-104045.
- [64] S. Torquato, F. H. Stillinger, Jammed hard-particle packings: From Kepler to Bernal and beyond, *Rev. Mod. Phys.* 82 (2010) 2633–2672. doi:10.1103/RevModPhys.82.2633.
- [65] C. F. Moukarzel, Elastic collapse in disordered isostatic networks, *Europhys. Lett.* 97 (2012) 36008. doi:10.1209/0295-5075/97/36008.
- [66] C. P. Goodrich, A. J. Liu, S. R. Nagel, Finite-size scaling at the jamming transition, *Phys. Rev. Lett.* 109 (2012) 095704. doi:10.1103/PhysRevLett.109.095704.
- [67] T. J. Rupert, Strain localization in a nanocrystalline metal: Atomic mechanisms and the effect of testing conditions, *J. Appl. Phys.* 114 (2013) 033527. doi:10.1063/1.4815965.
- [68] J. Schiøtz, K. W. Jacobsen, A maximum in the strength of nanocrystalline copper, *Science* 301 (2003) 1357–1359. doi:10.1126/science.1086636.
- [69] Y. Mishin, M. J. Mehl, D. A. Papaconstantopoulos, A. F. Voter, J. D. Kress, Structural stability and lattice defects in copper: Ab initio, tight-binding, and embedded-atom calculations, *Phys. Rev. B* 63 (2001) 224106. doi:10.1103/PhysRevB.63.224106.
- [70] G. Wu, K.-C. Chan, L. Zhu, L. Sun, J. Lu, Dual-phase nanostructuring as a route to high-strength magnesium alloys, *Nature* 545 (2017) 80–83. doi:10.1038/nature21691.
- [71] T. J. Rupert, J. R. Trelewicz, C. A. Schuh, Grain boundary relaxation strengthening of nanocrystalline Ni–W alloys, *J. Mater. Res.* 27 (2012) 1285–1294. doi:10.1557/jmr.2012.55.
- [72] W. Brostow, M. Chybicki, R. Laskowski, J. Rybicki, Voronoi polyhedra and Delaunay simplexes in the structural analysis of molecular-dynamics-simulated materials, *Phys. Rev. B* 57 (1998) 13448–13458. doi:10.1103/PhysRevB.57.13448.
- [73] E. Maras, O. Trushin, A. Stukowski, T. Ala-Nissila, H. Jónsson, Global transition path search for dislocation formation in Ge on Si(001), *Comput. Phys. Commun.* 205 (2016) 13–21. doi:

- [10.1016/j.cpc.2016.04.001](https://doi.org/10.1016/j.cpc.2016.04.001).
- [74] Y. Q. Cheng, E. Ma, Indicators of internal structural states for metallic glasses: Local order, free volume, and configurational potential energy, *Appl. Phys. Lett.* 93 (2008) 051910. doi:[10.1063/1.2966154](https://doi.org/10.1063/1.2966154).
- [75] J. Ding, Y.-Q. Cheng, E. Ma, Full icosahedra dominate local order in $\text{Cu}_{64}\text{Zr}_{34}$ metallic glass and supercooled liquid, *Acta Mater.* 69 (2014) 343–354. doi:[10.1016/j.actamat.2014.02.005](https://doi.org/10.1016/j.actamat.2014.02.005).
- [76] D. R. Nelson, Liquids and glasses in spaces of incommensurate curvature, *Phys. Rev. Lett.* 50 (1983) 982–985. doi:[10.1103/PhysRevLett.50.982](https://doi.org/10.1103/PhysRevLett.50.982).
- [77] D. R. Nelson, Order, frustration, and defects in liquids and glasses, *Phys. Rev. B* 28 (1983) 5515–5535. doi:[10.1103/PhysRevB.28.5515](https://doi.org/10.1103/PhysRevB.28.5515).
- [78] W. Schirmacher, G. Diezemann, C. Ganter, Harmonic vibrational excitations in disordered solids and the “boson peak”, *Phys. Rev. Lett.* 81 (1998) 136–139. doi:[10.1103/PhysRevLett.81.136](https://doi.org/10.1103/PhysRevLett.81.136).
- [79] W. Schirmacher, Thermal conductivity of glassy materials and the “boson peak”, *Europhys. Lett.* 73 (2006) 892. doi:[10.1209/epl/i2005-10471-9](https://doi.org/10.1209/epl/i2005-10471-9).
- [80] W. Schirmacher, B. Schmid, C. Tomaras, G. Viliani, G. Baldi, G. Ruocco, T. Scopigno, Vibrational excitations in systems with correlated disorder, *Phys. Status Solidi C* 5 (2008) 862–866. doi:[10.1002/pssc.200777584](https://doi.org/10.1002/pssc.200777584).

From metallic glasses to nanocrystals: Molecular dynamics simulations on the crossover from glass-like to grain-boundary-mediated deformation behaviour

Tobias Brink and Karsten Albe

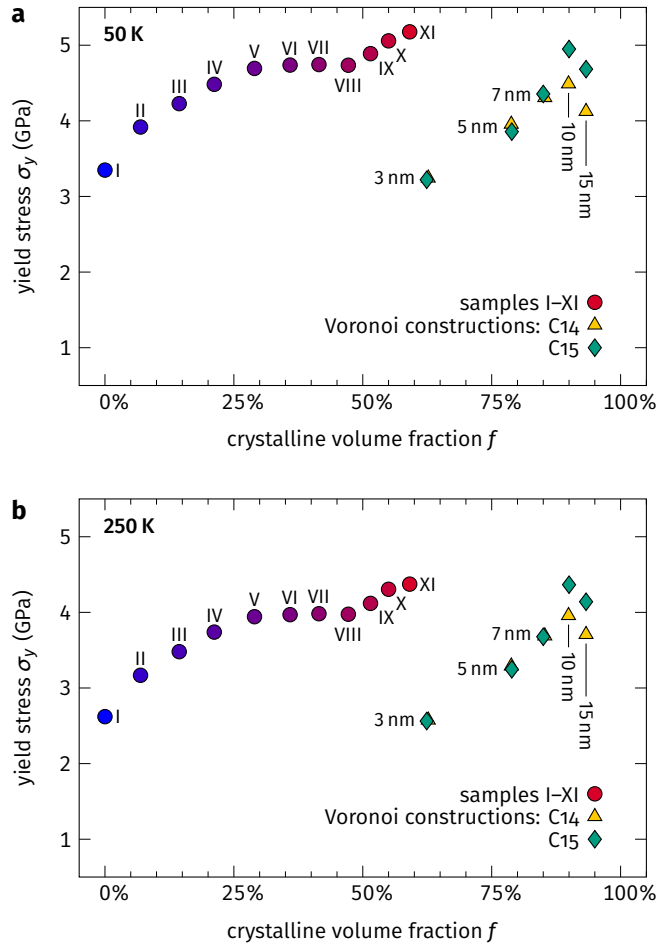


Figure S.1: Yield strength as a function of crystalline volume fraction for tensile tests at 50 K (a) and 250 K (b). The data points labelled I–XI refer to the samples with crystallites grown by annealing, while “Voronoi constructions” refers to artificially created polycrystals with different average grain sizes and crystal structures. Qualitatively, the behaviour is the same—independent of the temperature. Only the yield stress is uniformly reduced at 250 K.

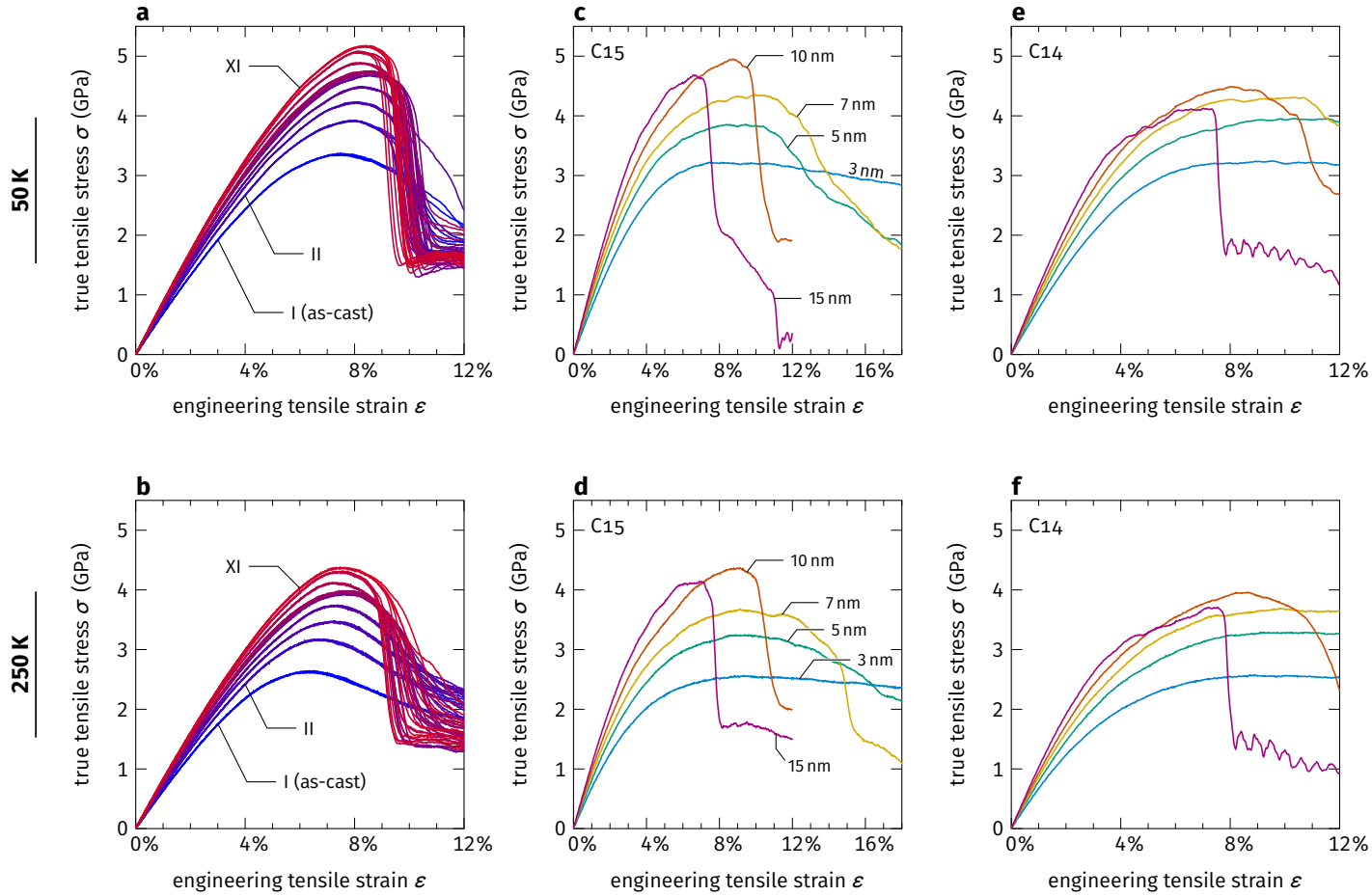


Figure S.2: Stress–strain curves of all samples.

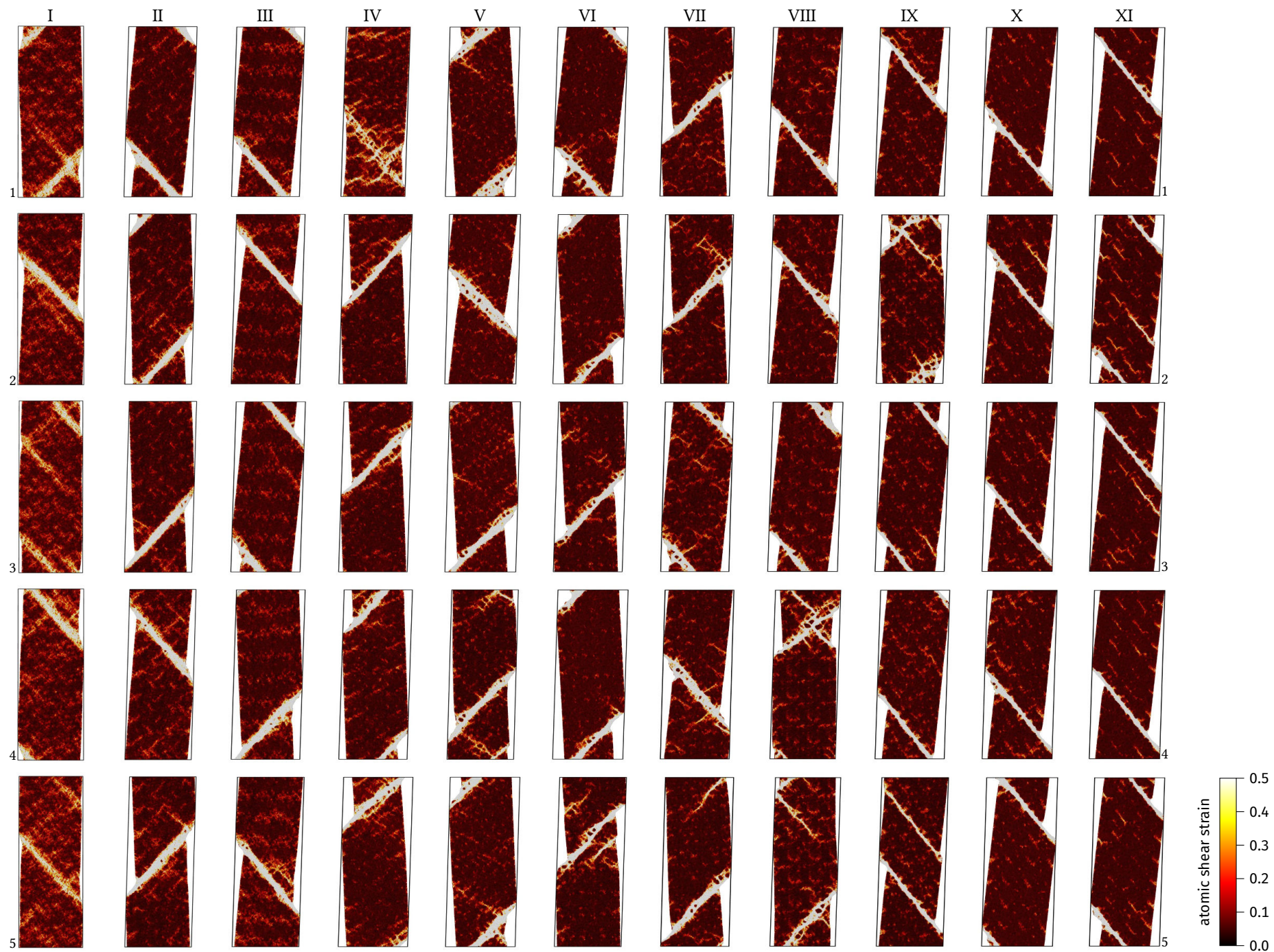


Figure S.3: Snapshots of samples after deformation at 50 K. Every row represents the results of a statistically independent run.

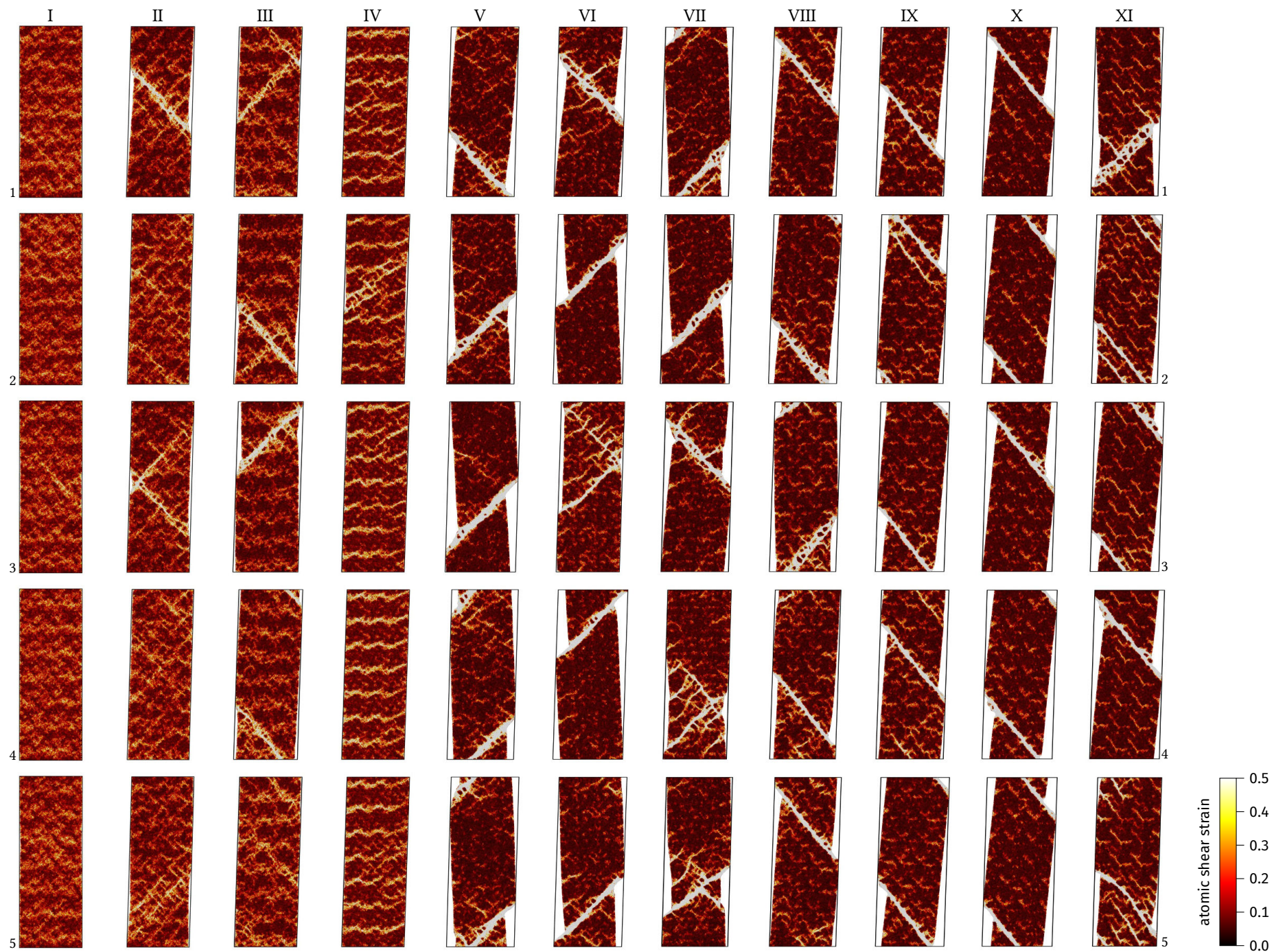


Figure S.4: Snapshots of samples after deformation at 250 K. Every row represents the results of a statistically independent run.

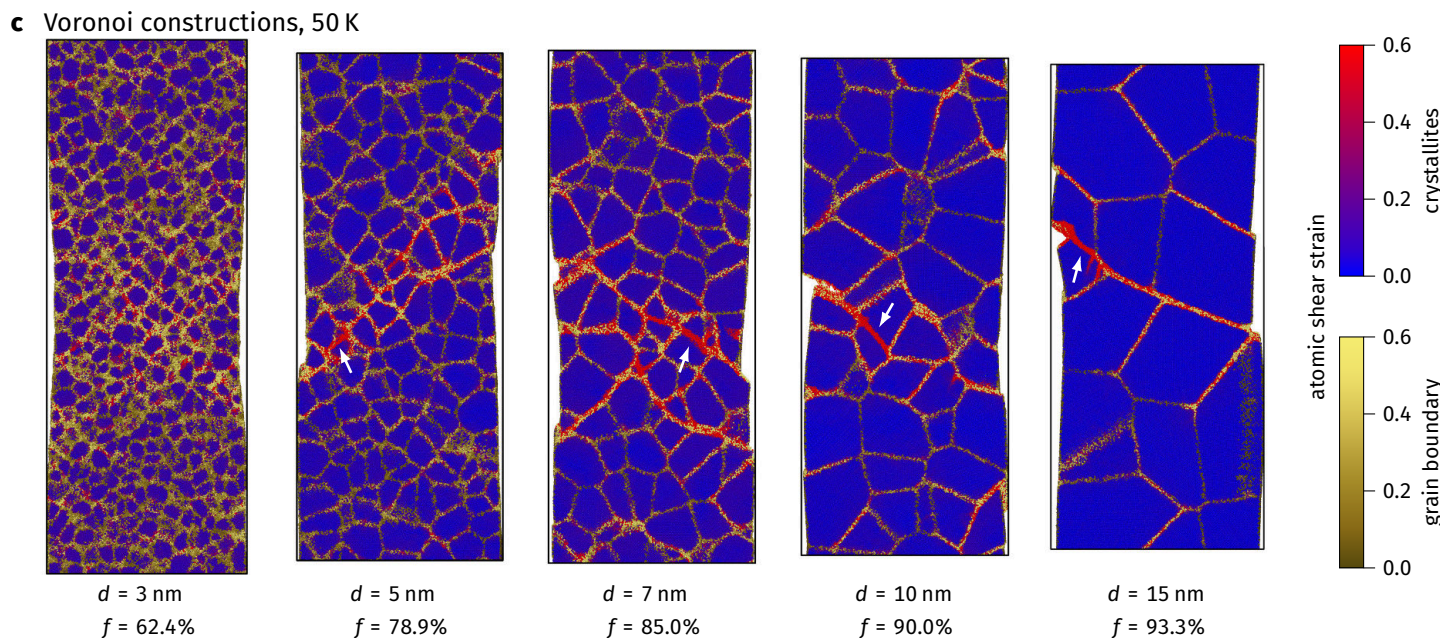
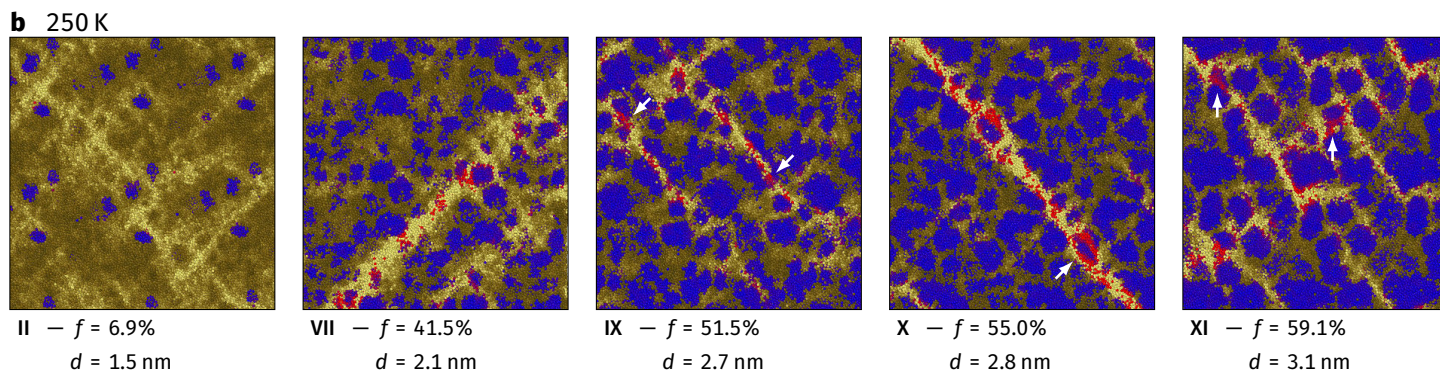
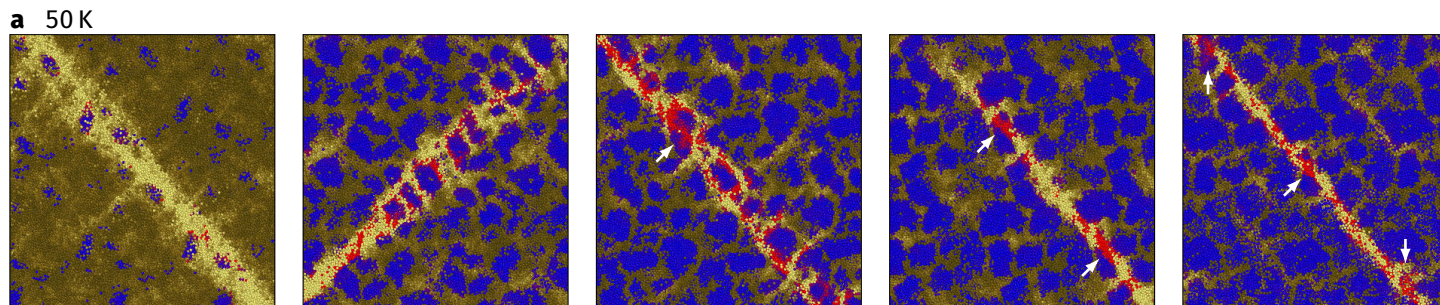


Figure S.5: Snapshots of selected samples after yield. The snapshots are coloured according to atomic strain, with different colour schemes for the crystallites and the amorphous phase. Arrows highlight where slip transfer from the amorphous phase into the crystallites takes place. (a) Detailed view of samples with crystallites grown by annealing, deformed at 50 K. Slip transfer and deformation of crystallites is only observed for large crystalline volume fractions. (b) The samples behave similar at 250 K, despite the reduced shear localisation. (c) The polycrystals by Voronoi construction usually exhibit localised deformation and slip transfer, except for the smallest grain size, at which a homogeneous grain-boundary-mediated flow occurs, which ultimately leads to necking. We only show samples with C15 crystal structure here, the C14 samples are qualitatively similar.

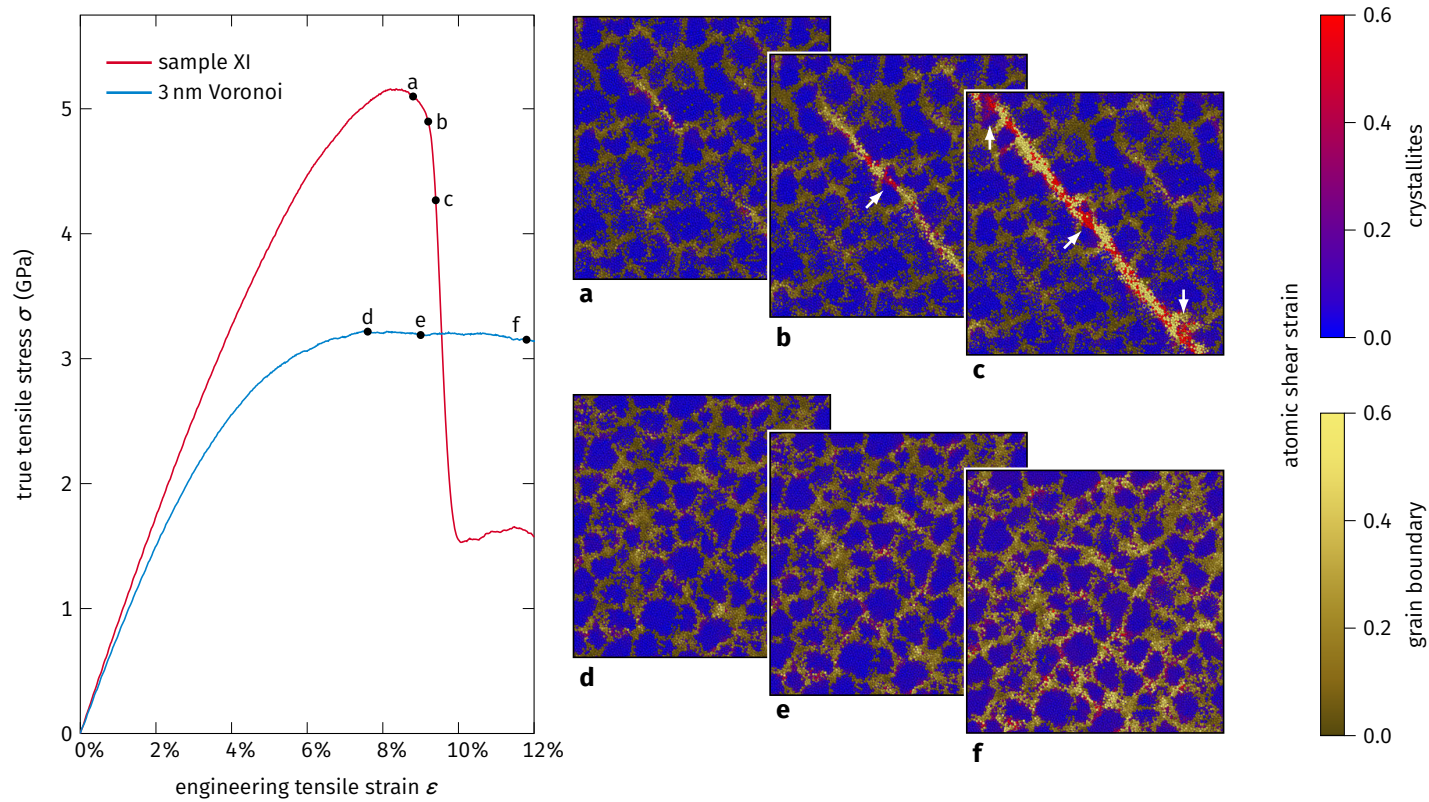


Figure S.6: Detailed yield process in sample XI and the Voronoi constructed sample with 3 nm C15 grains. Simulations performed at 50 K. (a) Yield in the relaxed sample starts in the amorphous phase, where it is confined by the surrounding crystallites. (b)–(c) The failure of the sample only occurs when the blocking crystallites are cut. (d)–(f) If the glass is less relaxed, though, the deformation is delocalised and purely grain-boundary-mediated flow can occur.

nanocrystalline copper

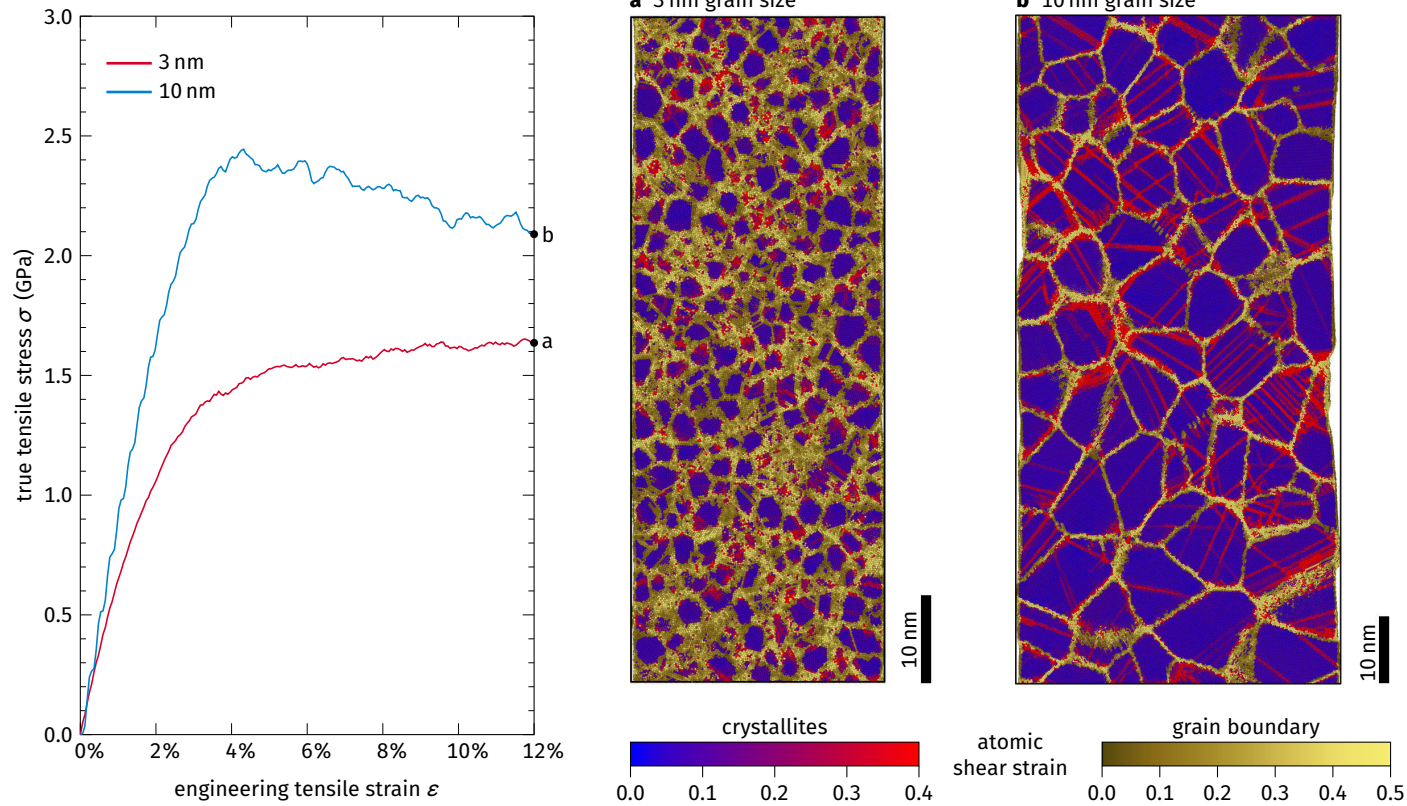


Figure S.7: Simulations of nanocrystalline copper with 3 nm and 10 nm grain sizes as an example of a ductile metal. The samples were created by Voronoi construction, minimised, equilibrated at 50 K for 1 ns, and finally deformed at 10^8 s^{-1} . Deformation at 3 nm grain size is predominantly localised in the grain boundary, while the crystallites participate at 10 nm grain size. These results are qualitatively similar to the unrelaxed $\text{Cu}_{64}\text{Zr}_{36}$ samples. A relaxation of the grain boundary is not possible, since massive grain growth sets in immediately.